Topographically organized representation of space and context in the medial prefrontal cortex

Jonas-Frederic Sauer*, Marlene Bartos*

University of Freiburg, Medical Faculty, Institute of Physiology I, Hermann-Herder-Strasse 7, D-79104 Freiburg, Germany.

*Correspondence: marlene.bartos@physiologie.uni-freiburg.de, jonas.sauer@physiologie.uni-freiburg.de

Abstract

Spatial tuning of pyramidal cells has been observed in diverse neocortical regions, but a systematic characterization of the properties of spatially tuned neurons across cortical layers and regions is lacking. Using mice navigating through virtual environments, we find topographical organizational principles for the representation of spatial features in the medial prefrontal cortex. We show that spatial tuning emerges across layers with a dorso-ventral gradient in the depth of spatial tuning, which resides in superficial layers. Moreover, the prefrontal cortex shows hemispheric lateralization of spatial tuning such that neurons located in the left hemisphere display more pronounced spatial tuning. During exploration of a novel compared to a familiar context, a different picture emerges. Context discrimination and familiarity detection is higher in superficial compared to deep layers. However, neurons of the right medial prefrontal cortex discriminate more efficiently between contexts than cells in the left hemisphere. Jointly, these results reveal a complex topographic organization of spatial representation and suggest a division of labor among prefrontal layers and subregions in the encoding of spatial position in the current environment and context discrimination.

Significance

The neocortex is composed of areas with specialized function (e.g. sensory vs. associational). Despite this functional diversity, emerging evidences suggest that the encoding of space might be a universal feature of cortical circuits. We identified distinct gradients of spatial tuning depth along the dorso-ventral and radial intrahemispheric and left-right interhemispheric axes. Moreover, neurons located in superficial layers in the right hemisphere show more pronounced context differentiation between a familiar and a novel environment. A complex topography of spatial tuning properties and context differentiation might thus support division of labor among medial prefrontal

cortical subnetworks to support local network computation relevant for the execution of context-dependent behavioral outcomes.

Introduction

Encoding of spatial information is classically assigned to the hippocampal-entorhinal system (1) (2) (3). However, with recent reports of spatially tuned neurons in the posterior parietal (4), retrosplenial (5), visual (6), and somatosensory cortex (7), as well as over large areas of the dorsal cortex including sensory and higher-order areas (8), it is becoming evident that spatially modulated activity is a more widespread phenomenon than initially assumed and might be a universal feature seen across the neocortex.

The medial prefrontal cortex (mPFC) is critical for cognitive functions such as the planning and execution of complex behaviors (9). Many cognitive tasks involving the mPFC require the simultaneous awareness of spatial variables including one's own current position in an environment, the recognition of novelty/familiarity of the surrounding features, and context discrimination (10) (11). In line with this, prefrontal neurons of mice display spatially tuned activities during cognitive tasks (12) (13) (14) (15) (16).

However, compared to the extensively studied properties of spatial coding in the hippocampal-entorhinal system it remains largely unclear whether mPFC neurons display spatially tuned activities across layers and subfields (17) as recently demonstrated for the retrosplenial cortex (5). Indeed, in the retrosplenial cortex spatial tuning is more pronounced in superficial than deep layers (5), whereas in the somatosensory cortex, spatially tuned neurons are prominently observed in deep layers (7), although systematic comparisons among layers are lacking. Distinct neocortical subfields furthermore receive different afferent inputs, including those from the hippocampal formation (18) (19), thus varying degrees of spatial tuning across subareas and layers might be expected. Furthermore, while the hippocampal place code rapidly emerges during exploration of

environments (20) (21), it is not clear how fast the neocortical spatial map is established once the animal is introduced to an arena.

Here, we addressed these questions by assessing spatial tuning in the mPFC across layers and subfields along the dorso-ventral axis while mice were navigating through virtual environments. We find that spatial tuning emerges rapidly upon context exposure, even in a novel arena. Moreover, we find pronounced topographical gradients of spatial modulation depth along the dorso-ventral and left right axes and a differential contribution of prefrontal layers to context differentiation. These data thus reveal a complex organization of neocortical spatial tuning properties along multiple prefrontal axes.

Results

Prefrontal neurons represent space during spontaneous unrewarded navigation

We trained head-fixed mice to run consecutive laps on a virtual circular track (1.5 or 2 m long; **Fig. 1**). The track was composed of linear segments with distinctive wall patterns and additional cues located outside the track (**Fig. 1A**). We chose this experimental setting to constrain the assessment of spatial tuning in one dimension (i.e. 1-D position on the track) and to avoid complex behaviours such as grooming or rearing, which are observed in freely moving mice and modulate the activity of prefrontal neurons (22). The animals moved along the track in a self-induced and self-paced manner without rewards. After familiarization to the track for several days, we recorded single units with linear silicon probes acutely lowered into the mPFC (**Fig. 1B**). To assess spatial representation, we quantified two parameters, sparsity and spatial information, from spatially binned firing rates of each neuron (8) (12). Sparsity quantifies the proportion of bins with average firing of at least 25% of the peak rate of each unit. Low values of this metric thus indicate that spiking activity is spatially confined to few bins on the track (**Fig. 1D**).

In total, we recorded from 1800 prefrontal neurons (*N*=17 mice). Based on spike waveform kinetics, we grouped the cells in putative pyramidal (*N*=1543) and GABAergic interneurons (*N*=257, **SI Appendix, Fig. S1**). Analysis of sparsity and spatial information during movement revealed a broad distribution for the pyramidal cell population, with many units displaying spatially confined activity (**Fig. 1C,D**). Both parameters were significantly different from a surrogate dataset created by shuffling the spike trains of each unit, indicating above-chance spatial representation by the population of prefrontal pyramidal neurons during spontaneous locomotion (Sparsity: $P=10^{-55}$; Spatial information: $P=1.5*10^{-21}$; **Fig. 1D**). Consistent with previous reports in spatial memory tasks (12), spatial tuning of prefrontal pyramidal units was lower than in the hippocampus under our experimental conditions ($P=0.002$; **Fig. 1E**). The firing of putative interneurons contained significant spatial information but spatial tuning was lower than in pyramidal cells (**SI Appendix, Fig. S1**). Further analyses showed significant stability of the spatial map within the recording session (**SI Appendix, Fig. S2**). In addition, spatial tuning was evident in population data extracted with principal component analysis (**SI Appendix, Fig. S3**).

To investigate the time course with which the spatial map emerged, we correlated for each pyramidal cell the average spatial tuning function with the spatially binned activity during individual runs (**Fig. 1F**). This analysis indicated a rapid onset of spatial tuning upon exposure to the virtual environment from the second run onwards. The activity of prefrontal neurons, particularly of pyramidal neurons, thus contains information about the position of the animal during spontaneous self-paced motion.

Spatial tuning emerges across prefrontal layers

To test whether spatial tuning properties differ among cortical layers, we quantified the laminar position of the silicon probes in the mPFC (**Fig. 2A**). During 34 recording sessions from 17 mice, the average sparsity and spatial information of all simultaneously recorded pyramidal cells per

session did not depend on laminar depth (**Fig. 2B**, sparsity: P=0.621, spatial information: P=0.257, recording depth ranged from 199 to 714 µm). Both layer 2/3 and layer 5/6 pyramidal cells were spatially tuned as they displayed significant sparsity (layer 2/3: $P=1.6*10^{-11}$, N=233 cells, 4 mice; layer 5/6: $P=1.3*10^{-8}$, N=311 cells, 7 mice, recordings from the left hemisphere) and spatial information content (layer 2/3: P=0.0004, layer 5/6: P=0.002, **Fig. 2C**) compared to shuffled controls. Comparisons of sparsity of cells recorded in layer 2/3 with those recorded in layer 5/6 revealed no significant difference (P=0.112, **Fig. 2C**). However, we found higher average spatial information in layer 2/3 neurons (P=0.03, **Fig. 2C**). Since sparsity and spatial information both showed an inverse correlation with firing rate, unequal firing rates might confound the comparison of spatial tuning properties among cortical layers (**SI Appendix, Fig. S4**). Indeed, layer 2/3 neurons discharged at lower average rates during movement on the track than layer 5/6 cells (layer 2/3: 2.4 ± 0.2 Hz, layer 5/6: 3.3 ± 0.3 Hz, P=0.007, **Fig. 2D**). We therefore examined whether distinct spatial tuning properties persist when we consider a population of neurons with equal firing rate. To address this question, we performed an iterative procedure in which a random subset of layer 5/6 neurons was drawn from the total population of cells, and spatial parameters were compared to the layer 2/3 population only if the two groups showed similar mean firing rates during running on the virtual maze (P>0.05 for the comparison of rates; **Methods**). In 1000 rate-matched iterations, no cases of significantly different sparsity were observed, and spatial information showed a significant difference in only 35.1% of iterations (**Fig. 2E**). Thus, our analysis indicates that comparisons of superficial and deep layer neuronal populations with matching firing rate show similar spatial information contents.

To further rule out layer-specific spatial modulation, we performed simultaneous recordings at two cortical depths using multi-shank probes (shank spacing 250 µm, **Fig. 2F,G**). Sparsity, spatial information and firing rate did not depend on cortical depth in these recordings (sparsity: P=0.629, spatial information: P=0.204, rate: P=0.563, pairwise comparison between simultaneously recorded

superficial and deep shanks, *N*=6 sessions from 3 mice, **Fig. 2G**). These data jointly show similar spatial tuning across cortical layers of the mPFC.

A dorso-ventral gradient of spatial representation

Hippocampal inputs transfer spatial information to the mPFC network (10). Tracing studies indicated that hippocampal projections to the mPFC show the highest density in ventral medial prefrontal areas (23) (24) (25) (26). We therefore hypothesized that spatial tuning of mPFC neurons might depend on their position along the dorso-ventral axis of the mPFC (**Fig. 3**). Linear silicon probes allow pinpointing the location of the recorded units based on the amplitude of the extracellular waveform on neighboring electrodes, enabling us to determine the position of each recorded pyramidal neuron along the dorso-ventral axis (ranging from accessory motor cortex/cingulate cortex to prelimbic/medial orbital cortex). Consistent with hippocampal projections, we found a higher power of theta (6-12 Hz) oscillations in ventral mPFC areas (Spearman's r = -0.995, $P=10^{-63}$, **Fig. 3B,C**). Unexpectedly, when we binned the neurons in those located on the top or bottom 300 µm of the shank (corresponding to accessory motor/cingulate cortex and prelimbic/medial orbital cortex, respectively, **Fig. 3D**), we found lower sparsity of units belonging to the dorsal group (*P*=0.0002, *N*=337 dorsal and 265 ventral neurons; **Fig. 3E**). There was furthermore a trend towards higher spatial information content of dorsal neurons, which did not reach significance (*P*=0.094; **Fig. 3E**). Firing rate (*P*=0.326) and strength of coupling to theta oscillations (*P*=0.7) did not differ between dorsal and ventral neurons. Thus, our data suggest stronger spatial tuning of neurons in the dorsal mPFC based on their sparsity.

Since the recordings contained neurons from superficial and deep layer layers, we speculated that layer-dependent differences might attenuate potential dorso-ventral gradients in spatial tuning. We therefore separately analyzed layer 2/3 (*N*=125 dorsal and 104 ventral neurons) and layer 5/6 cells (*N*=212 dorsal and 161 ventral neurons, **Fig. 3F-K**). In superficial layers, we

detected a prominent dorso-ventral gradient in sparsity and spatial information, with stronger spatial tuning in the dorsal mPFC (Sparsity: P=6.4*10^{-6}, Spatial information: P=0.007, **Fig. 3F**). Since layer 2/3 cells in the dorsal mPFC showed higher firing rates than the ones in the ventral group (P=0.011), we applied the rate-matching iteration procedure. This analysis revealed a significant difference between dorsal and ventral neurons in sparsity in 100% and in spatial information in 78% of rate-matched comparisons (1000 iterations, **Fig. 3G**), further confirming higher spatial tuning of dorsal mPFC cells. In agreement with the observed dorso-ventral gradient in spatial tuning depth, dorsally located neurons in superficial layers showed significantly stronger theta-coupling compared to ventrally located cells (P=0.035, **Fig. 3H**). In contrast, recordings from deep layers showed no difference in sparsity (P=0.176) or spatial information (P=0.972) along the dorso-ventral axis (**Fig. 3I,J**). In contrast to layer 2/3 neurons, ventrally located cells in deep layers were more strongly entrained by theta activity patterns than superficial neurons (P=0.003, **Fig. 3K**). Jointly, these data point to a dorso-ventral gradient in spatial tuning depth of cells in superficial layers of the mPFC.

Hemispheric asymmetry of spatial representation

The observed dorso-ventral gradient in spatial modulation depth motivated us to search for additional topographical rules of spatial representation. Prefrontal cognitive functions in humans are highly lateralized (27) (28) (29). Therefore, we examined whether the properties of spatial representation might differ between the left and right mPFC (**Fig. 4**). We observed significantly lower sparsity (P=8.9*10^{-22}) and higher spatial information in neurons recorded in the left compared to the right mPFC (P=4.4*10^{-13}, N=544 and 639 neurons from 11 and 8 mice in left and right mPFC, respectively; data were pooled across layers; **Fig. 4A**). There was furthermore a lower average firing rate in left prefrontal neurons (P=0.008, **Fig. 4A**). Rate-matching analysis revealed that the effects of lower sparsity and higher spatial information were also evident when accounting

for rate differences in 100% of iterations (**Fig. 4B**). Furthermore, theta-coupling depth was higher in the left versus the right mPFC (P=0.004; **Fig. 4C**). Thus, our data indicate stronger spatial tuning in the left hemisphere.

Since we identified dorso-ventral differences in spatial tuning in superficial but not deep layers (**Fig. 3F**), we restricted our further analysis to recordings from layers 5/6 (N=311 and 639 neurons from 7 and 8 mice for left and right mPFC, respectively). Similar to the full dataset, this analysis showed lower sparsity ($P=1.8*10^{-12}$), higher spatial information ($P=4.5*10^{-7}$) and stronger theta entrainment in the left mPFC (P=0.046), while firing rates were similar (P=0.407; **Fig. 4D,E**). To rule out the potential influence of inter-individual differences, we further restricted our analysis to mice from which recordings from both left and right cortex had been performed sequentially over subsequent days (N=142 and 213 neurons from 3 mice). Again, sparsity was lower ($P=1.2*10^{-14}$), while spatial information ($P=5.3*10^{-6}$) and theta coupling depth were higher in the left compared to the right mPFC ($P=2.7*10^{-5}$; **Fig. 4F,G**). Thus, these data indicate interhemispheric asymmetries with pyramidal neurons in the left mPFC displaying more prominent spatial tuning properties than the ones in the right mPFC.

Topographical gradients in representational stability

Finally, we assessed context differentiation and stability of spatial tuning by sequentially exposing mice to a familiar (fam) and an additional novel unfamiliar circular track (nov), and compared the data with a re-exposure to the same familiar (fam') track within one recording session (**Fig. 5**). The novel track differed from the familiar environment in size (track length 3 m) and visual features (colors, wall patterns, external cues, **Fig. 5A**). We previously demonstrated that mice are capable to recognize such novel virtual tracks (30). Analysis of waveform parameters indicated stable recording conditions throughout the exposure to the three environments (**SI Appendix, Fig. S5**). Since spatial tuning of prefrontal neurons during exposure to a novel track has not been

characterized, we first quantified the spatial tuning properties of all pyramidal neurons irrespective of their anatomical position. Pyramidal neurons showed significant sparsity and spatial information compared to shuffled datasets in all three conditions (**Fig. 5C**), indicating spatial tuning on the novel track. The neurons displayed comparable average firing rates during running in all three experimental conditions (**SI Appendix, Fig. S5**). To assess remapping of pyramidal neurons during exposure to novelty, we quantified the correlation coefficient of the mean occupation-normalized spatially binned firing rates for each neuron (spatial stability). Spatial stability between fam and nov was low (mean correlation 0.048 ± 0.008, $P<0.05$; **Fig. 5D**). Given that spatial tuning is observed in both fam and nov conditions (**Fig. 5C**), these data suggest that exposure to a novel environment leads to a rearrangement of spatial representation in the mPFC. During exploration of nov, correlation of the spatial tuning function during individual runs to the average map of each neuron revealed that spatial tuning was significantly different from shuffled data from the second lap onwards (**Fig. 5E**). Spatial representation thus rapidly remaps during exploration of the novel track. During re-exposure to fam', we found a much higher correlation to the original spatial pattern observed in fam (mean correlation: 0.210 ± 0.01, $P<0.05$; **Fig. 5D**), indicating that the spatial representation of the original environment is partially reinstated upon re-exposure to the same arena. Consistent with this observation, analysis of spatially binned population dynamics revealed a higher spatial correlation between fam and fam' compared to fam and nov (**SI Appendix, Fig. S5**).

Having characterized the basic properties of spatial tuning during nov and fam' exploration, we next investigated whether the stability of the spatial map across the three environments is shaped by topographic properties. With regard to superficial and deep layers, we found stronger remapping (i.e. a lower correlation of the spatial tuning function) between fam and nov in superficial compared to deep layer neurons (**Fig. 5F**, $P=0.047$, $N=162$ layer 2/3 and 142 layer 5 pyramidal neurons; we restricted this analysis to recordings from the left hemisphere to exclude inter-hemispheric differences as a confounding factor). Furthermore, stability between fam and fam' was significantly

higher in layer 2/3 (P=0.0003, **Fig. 5F**). These data indicate that superficial layers remap more strongly during novel context exploration and reactivate the original spatial tuning more efficiently during re-exposure to the familiar environment.

Next, we assessed whether position along the dorso-ventral axis relates to context recognition. In contrast to the apparent dorso-ventral gradient of spatial tuning in layer 2/3, we found no difference in tuning correlation between fam and nov (P=0.290, N=47 and 28 dorsal and ventral cells, respectively) or fam and fam' (P=0.729) for dorsally or ventrally located neurons (we restricted this analysis to layer 2/3 recordings from the left hemisphere to exclude inter-hemispheric differences as a confounding factor, **SI Appendix, Fig. S6**).

Finally, we assessed spatial tuning during nov and fam' in recordings from the left and right mPFC (we restricted the analysis to deep layer neurons to exclude layer differences as a confounding factor). Stability between fam and nov was significantly higher in the left compared to the right mPFC (P=0.045, N=142 and 509 neurons recorded in the left and right mPFC, respectively), suggesting stronger remapping in the right hemisphere. Furthermore, spatial stability between fam and fam' was significantly higher in the right mPFC (P=2.9*10^{-8}, **Fig. 5G**). Thus, our data suggest that the right mPFC discriminates better between familiar and novel environments and reactivates the original spatial tuning pattern more efficiently upon return to the familiar space.

Discussion

Here we show that the mPFC of mice displays detectable spatial tuning during spontaneous, self-paced motion, including the representation of position as well as context. In line with findings of grid cells in the human cortex (31) (32) and spatially modulated cells in the cortex of rodents (4) (5) (6) (7) (8), our findings are consistent with a more general neuronal system tracking spatial variables in neocortical columns (33). Our data further demonstrate that in the mPFC distinct

features of spatial representation occur lateralized and along dorso-ventral and superficial-deep radial gradients.

The stronger spatial tuning of the dorsal mPFC is surprising since multiple studies demonstrated denser innervation of the ventral PFC by hippocampal inputs (23) (24) (25) (26), which presumably composes the primary source of spatial information to the mPFC (10). Direct projections from the ventral CA1 furthermore terminate in deep cortical layers, particularly in dorsal parts of the mPFC (23) (26). Moreover, optogenetic activation of direct hippocampal afferents to the mPFC revealed stronger synaptic drive to layer 5 than to layer 3 neurons of the prelimbic cortex (26). In addition to direct hippocampal afferents, spatially modulated inputs reach the mPFC via the thalamic nucleus reuniens, which relays hippocampal afferents to the mPFC (14) (34). However, similar to the direct hippocampal inputs, nucleus reuniens afferents have also been shown to preferentially target ventral prefrontal areas (34). Our findings of a dorso-ventral gradient of spatial tuning in superficial but not deep layers of the mPFC is thus not likely explained by direct hippocampal input. In fact, deep layer neurons located ventrally are more strongly entrained by theta oscillations, as one would predict based on the anatomy of hippocampal inputs. In contrast, superficially located neurons are more strongly theta-coupled when they reside in dorsal parts of the mPFC. We thus propose that the spatial tuning of prefrontal neurons is only partly contingent on direct hippocampal input. Lesioning the hippocampus indeed reduced spatial information of neocortical cells and decreased position decoding accuracy based of spatially tuned neocortical neurons but did not entirely eliminate spatial tuning in the neocortex (8), consistent with an additional hippocampus-independent mechanism. Tracing studies confirmed the presence of entorhinal cortex projections in the dorsal and ventral portions of the mPFC (35) (36), which might contribute to spatial tuning properties of mPFC cells. In addition, spatial signals might reach the mPFC via other cortical areas. For instance, prominent spatial tuning features have been observed in the somatosensory cortex (7), which projects monosynaptically to the mPFC (18). Only few

connections from the hippocampal formation to the somatorsensory cortex have been identified (25), which gave rise to the hypothesis that the somatosensory cortex might contain a hippocampus-independent spatial navigation system (7). It remains to be tested whether the complex topographical nature of prefrontal spatial tuning emerges due to complementary inputs from the hippocampal and somatosensory spatial navigation systems.

Our data revealed a lateralization of spatial representation, with stronger spatial tuning properties in the left but more pronounced familiarity detection in the right mPFC. Prefrontal lateralization has been demonstrated using functional imaging in human participants and showed that hemispheric specialization depends on the nature of the task (37). While left prefrontal regions are considered to be involved in processing the 'verbal domain', the right prefrontal cortex processes visuo-spatial information (27). Furthermore, the left prefrontal cortex has been associated with drawing logical and causal inferences while the right prefrontal area has been implicated in the detection of inconsistencies between pre-existing beliefs and new information (29). In line with the distinct function of the left and right PFC in humans and reports of lateralization in mouse auditory cortex (38) as well as hippocampus (39) (40), we propose a functional division of labor between left and right mPFCs in mice such that the dorsal part of the left prefrontal hemisphere might be best suited to integrate the own position in space, whereas the dorsal right mPFC might support the differentiation between familiarity and novelty (**Fig. 5H**). The mechanisms of differential spatial tuning properties of both mPFCs remain elusive. Activity in the left but not right CA3 has been reported to be required for spatial memory (40), and long-term plasticity of CA3 outputs in CA1 occur only on synapses originating from the left but not right CA3 (41). While these data suggest pronounced lateralization within the hippocampal circuitry, potential hemispheric asymmetries in CA1 output to the neocortex are much less understood. Based on our data we predict that axons from the left CA1 will contain more spatial information than axons from the right CA1 (projections

to the mPFC are ipsilateral), while similarity during context re-exposure will be higher in the right CA1 output.

Our data reveal prominent remapping in the mPFC during exploration of a novel arena reminiscent of dynamic changes observed in CA1 pyramidal neurons upon exposure to a novel arena (30) (42). We further find a dissociation of spatial tuning per se and remapping properties such that superficial and deep layers show comparable spatial tuning while superficial layers discriminate contexts more efficiently. Stronger context discrimination in superficial layers might relate to the integration of rich intra-cortical inputs in sparsely active layer 2/3 neurons. Similar to the known high selectivity of superficial layer cells in sensory cortices for stimulus properties (43) (44), context specificity might be the analog of prefrontal responses in layer 2/3 during contextual changes (the environment being the stimulus property in this sense).

In summary, our work indicates that in the absence of particular cognitive task demands the prefrontal cortex represents spatial and contextual information in a layer- and hemisphere-dependent manner. Such a division of labor among medial prefrontal cortical subnetworks may be important in supporting local network computation relevant for the execution of context-dependent behavioral outcomes. Further investigations of area-specific mPFC circuits during cognitive tasks, resolving distinct layers, dorso-ventral subregions, as well as the left and right hemisphere's subnetworks will help to understand their contribution to cognitive behavior.

Materials and Methods

Mice

C57Bl6/J mice of both sexes were maintained on a 12h dark-light cycle with free access to food and water. At the start of the experiment, the animals were 6 to 13 weeks old. All experiments were performed in agreement with national legislation and were approved by the Regierungspräsidium Freiburg.

Surgical procedures

For single-unit recording in the virtual reality, a stainless steel head plate was implanted on the skull under general anesthesia in isoflurane (induction: 3%, maintenance: 1-2%) using dental cement. The animals were allowed to recover from head plate implantation for at least three days. Buprenorphin (0.1 mg/kg body weight) and Carprofen (5 mg/kg body weight) were injected subcutaneously before the surgery for pain relief. Once the animals were habituated to head-fixation (see below), a craniotomy was performed over both mPFCs (1.9 mm anterior, 0.4 mm lateral of bregma) under isoflurane anesthesia. The craniotomy was then sealed of with QuikCast elastomer until the recordings took place. An additional injection of Carprofen was given for analgesia prior to craniotomy.

Single-unit recording in the virtual reality

After recovery from head-plate implantation, the mice were trained to run on a circular track in a virtual reality. They were briefly sedated with isoflurane applied in oxygen and head-fixed such that they could comfortably stand on a circular styrofoam weel. First, animals were habituated to head-fixation without the virtual reality turned on. After at least three days of habituation, training in the virtual reality (circular track, length 1.5 m or 2 m, visual cues placed outside the arena) was conducted. The virtual reality was constructed with open-source 3D rendering software Blender

(45) and was projected on five computer screens surrounding the head-fixation setup. Over subsequent days, mice were accustomed to the virtual environment until the animals appeared calm and traversed the circular maze reliably.

Recordings were performed in the arena to which the animals were habituated (*N*=17 mice mPFC, *N*=2 mice CA1). The animals completed on average 21.8 ± 5.3 laps per recording session. In a subset of mice (*N*=8 animals), we additionally exposed the animals within the same session to a novel arena (nov, 13.8 ± 2.2 laps completed), which the mice encountered for the first time during the initial recording session. The novel arena differed in size (3 m circle length) and visual features from the familiar arena. After recording in the novel arena, the animals were again exposed to the familiar track to assess the reactivation of spatially tuned activities in the familiar context (15.4 ± 4.3 laps were completed on average).

Recordings were conducted 1-3 days after the craniotomy. A single-shank silicon probe with 64 recording sites (electrode pitch 20 µm, total shank length 1275 µm, H3 probe, Cambridge Neurotech) coated with a fluorescent marker (DiI or DiO) was slowly (~2-5 µm/s) lowered to the mPFC (1800-1900 µm below brain surface). In three mice, a four shank probe with 16 electrodes per shank (Cambridge Neurotech) was used to perform simultaneous recordings from different neocortical layers. After insertion, the probe was left in place before starting the recording for 10-15 min. In two mice, recordings were obtained from hippocampal CA1. Wide-band neural signals were recorded at 30 kHz sampling with a 64-channel amplifier (Intan Technologies) connected to an USB acquisition board (OpenEphys). The position in the virtual reality was recorded as a pulse-width modulated signal using one of the analog input channels of the OpenEphys USB interface board. After recording, the silicon probe was slowly retracted and the craniotomy sealed off with QuickCast elastomer. 1-2 recording sessions were performed with each animal, with one session per day.

Histology

After the last recording session, the animals were deeply anesthetized with an intraperitoneal injection of ketamin/xylazine and transcardially perfused with ~20 ml phosphate-buffered saline followed by ~30 ml of 4% paraformaldehyde. After post-fixation over night, 100 µm-thick frontal sections of the mPFC were cut, washed several times in phosphate-buffered saline (PBS) and stained with 4′,6-diamidino-2-phenylindole. The location of the silicon probe was visualized with a laser-scanning microscope (LSM 710 or 900, Zeiss) following the nomenclature of the Allen Brain Atlas. To determine laminar depth of the probe, the distance from pia to the shank was measured orthogonal to the cortical layers.

Single-unit isolation

Single unit clusters were isolated from bandpass-filtered raw data (0.3-3 kHz) using MountainSort (46). Putative single-unit clusters that fulfilled quality criteria of high isolation index (>0.90) and low noise overlap (<0.1) were kept for manual curation, during which only clusters with a clear refractory period and clean waveform shape were saved for further analysis. In case of two clusters with similar waveforms, cross-correlation was used to assess whether clusters had to be merged. Isolated units were separated in putative excitatory and inhibitory neurons based on trough-to-peak duration and asymmetry index (47) using k-means clustering. To quantify the stability of single-unit recording during the recording sessions, waveforms of the channel with the largest voltage deflection were average separately for the time the animal explored the familiar track and during re-exposure to the familiar track after completion of running on the novel track. Stability was assessed by calculating Pearson’s correlation coefficient between the waveforms of each unit during both conditions and by correlating the peak amplitude recorded during both sessions. To extract the physical location of the units, the channel on the silicon probe with the largest negative amplitude

deflection was defined as the location of the unit and matched to histological data. All spike analysis was performed during times when the animal was moving at a speed of at least 2 cm/s.

Analysis of single unit data

Spike data was first aligned to the position signal in the maze. For that, the pulse-width modulated signal indicating position was transformed to a continuous signal ranging from 0 to 1 (denoting start and end of a complete circle) by low-pass filtering and manual curation of start and end points. Firing rate during movement on the maze was estimated by taking all spikes during which the minimum speed criterion was fulfilled and dividing them by the total time spent moving. To obtain sparsity, the spiking of individual units was binned as a function of space on the circular maze (40 bins) and normalized by occupancy of each bin. Sparsity was defined as the proportion of bins with at least 25% of the spike frequency of the bin with maximal firing activity (12). Spatial information *SI* was calculated as

$$SI = \sum_{i=1}^{N} p_i \frac{f_i}{f} \log_2 \frac{f_i}{f} \quad ,$$

where N is the number of bins, p is the occupation probability in the ith bin, f_i is the activity in bin i, and f is the average activity of the neuron across bins (8). A control data set was constructed for each recording session by shuffling the inter-spike intervals of each neuron before spatial binning. To determine spatial consistency within the session, average occupancy-normalized spatial histograms of spikes were constructed separately for the first and last six runs of a given recording session. Consistency was then defined by Pearson's correlation coefficient between both histograms and computed for each unit. For spatial stability, average spike rates as a function of position on the maze (40 bins) were obtained for fam, nov and fam'. Stability was defined as Pearson's r computed for the average spatial maps. Control data were generated by shuffling the interspike intervals of

each neuron. In case of single-run correlations, Pearson's r was computed separately for all possible run pairs within fam, between fam and nov, or between fam and fam' in a round-robin fashion and averaged across runs.

Theta coupling was assessed by first extracting the phase of the 6-12 Hz-filtered local field potential of all spikes during running, selecting cells with non-uniform phase distributions using Rayleigh's test, and computing the pairwise phase consistency *PPC* as

$$PPC = \frac{\pi - 2D}{\pi},$$

where *D* is the average pairwise circular distance between individual spikes as

$$D = \frac{2}{N(N-1)} \sum_{j=1}^{N-1} \sum_{k=(j+1)}^{N} d(\theta_j, \theta_k),$$

where θ_j and θ_k are the phases of the local field potential of spikes *j* and *k*, and *N* is the total number of spikes of the unit. Theta power was computed using Welch's method with a window size of 10 s and 10x zero-padding.

<u>Principal component analysis</u>

Binned spike trains of single units (bin width 30 ms) were square-root transformed and smoothed with a Gaussian kernel of s.d. 50 ms (48). Neurons with low mean firing rate <1 Hz were excluded from this analysis (48). A control data set was constructed for each recording session by shuffling the inter-spike intervals of each pyramidal neuron before binning. For each session, principal component analysis was then applied to the *N* by *B* array containing spike data of *N* neurons in *B* bins, thus resulting in *N* principal components. To obtain time-resolved population dynamics, the smoothed spike trains were projected onto the principal components *C*, giving a *C* x *B* array of population dynamics over time. Each component vector was binned as a function of location for each run on the maze (40 bins). To determine spatial variance, all runs of a session were averaged separately for the leading ten components. The standard deviation of the spatially binned

population activity was determined and averaged across components, weighted by the explained variance of the respective component. To obtain spatial consistency, the first and last six runs were averaged separately for the leading ten components. Then, for each component, the spatial correlation was determined as Pearson's correlation coefficient. Lastly, the spatial correlation was averaged across components, while weighting by the explained variance of each component. To determine single run consistency, we computed the spatial correlation between individual runs that occurred between one and ten runs apart from each other. Correlations between all possible combinations of run pairs in each distance category were averaged separately for each component. Finally, an average across the leading ten components was obtained while weighting with the explained variance of the component. The same analysis was also performed for individual units by taking their binned firing as a basis for single-trial correlation.

Statistical analysis

Sample sizes for most comparisons of single unit data were large ($>N=50$). Comparisons were done with two-sided Welch's tests, which is robust against deviation from normal distribution at large sample sizes (49). In cases of smaller sample sizes, comparisons were performed with a Mann-Whitney U-test if the data did not follow a normal distribution, otherwise an unpaired *t*-test was used. Normality was assessed with a Shapiro-Wilk test. Correlations between spatial tuning functions were tested with Pearson's correlation coefficient to detect linear correlations. Correlations for which linearity could not be assumed (e.g. cortical depth *vs.* spatial information) were assessed with Spearman's correlation coefficient. Pairwise comparisons of spatial tuning parameters for simultaneous recordings were done with a paired *t*-test. Significant theta coupling was assessed with Rayleigh's test for circular uniformity. Data are presented as full data ranges with means (violin plots) or as mean ± sem where indicated. All analysis (except for initial spike sorting, see above) including statistics were performed in Python2.7.

Acknowledgments

We thank Johannes Letzkus, Jozsef Csicsvari and Antje Kilias for critical comments on earlier versions of the manuscript, and Kerstin Semmler and Karin Winterhalter for technical assistance.

References

1. C. Wang, X. Chen, J. J. Knierim, Egocentric and allocentric representations of space in the rodent brain. *Curr. Opin. Neurobiol.* **60**, 12–20 (2020).

2. T. Hafting, M. Fyhn, S. Molden, M.-B. Moser, E. I. Moser, Microstructure of a spatial map in the entorhinal cortex. *Nature* **436**, 801–806 (2005).

3. T. Solstad, C. N. Boccara, E. Kropff, M.-B. Moser, E. I. Moser, Representation of Geometric Borders in the Entorhinal Cortex. *Science* **322**, 1865–1868 (2008).

4. C. D. Harvey, P. Coen, D. W. Tank, Choice-specific sequences in parietal cortex during a virtual-navigation decision task. *Nature* **484**, 62–68 (2012).

5. D. Mao, S. Kandler, B. L. McNaughton, V. Bonin, Sparse orthogonal population representation of spatial context in the retrosplenial cortex. *Nat Commun* **8**, 243 (2017).

6. A. Fiser, *et al.*, Experience-dependent spatial expectations in mouse visual cortex. *Nat Neurosci* **19**, 1658–1664 (2016).

7. X. Long, S.-J. Zhang, A novel somatosensory spatial navigation system outside the hippocampal formation. *Cell Research*, 1–15 (2021).

8. I. M. Esteves, *et al.*, Spatial Information Encoding across Multiple Neocortical Regions Depends on an Intact Hippocampus. *J Neurosci* **41**, 307–319 (2021).

9. A. Diamond, Executive Functions. *Annual Review of Psychology* **64**, 135–168 (2013).

10. T. Spellman, *et al.*, Hippocampal-prefrontal input supports spatial encoding in working memory. *Nature* **522**, 309–314 (2015).

11. J. J. Tuscher, L. R. Taxier, A. M. Fortress, K. M. Frick, Chemogenetic inactivation of the dorsal hippocampus and medial prefrontal cortex, individually and concurrently, impairs object recognition and spatial memory consolidation in female mice. *Neurobiol Learn Mem* **156**, 103–116 (2018).

12. M. C. Zielinski, J. D. Shin, S. P. Jadhav, Coherent Coding of Spatial Position Mediated by Theta Oscillations in the Hippocampus and Prefrontal Cortex. *J. Neurosci.* **39**, 4550–4565 (2019).

13. S. Fujisawa, A. Amarasingham, M. T. Harrison, G. Buzsáki, Behavior-dependent short-term assembly dynamics in the medial prefrontal cortex. *Nat. Neurosci.* **11**, 823–833 (2008).

14. H. T. Ito, S.-J. Zhang, M. P. Witter, E. I. Moser, M.-B. Moser, A prefrontal-thalamo-hippocampal circuit for goal-directed spatial navigation. *Nature* **522**, 50–55 (2015).

15. M. W. Jung, Y. Qin, B. L. McNaughton, C. A. Barnes, Firing characteristics of deep layer neurons in prefrontal cortex in rats performing spatial working memory tasks. *Cerebral Cortex (New York, N.Y.: 1991)* **8**, 437–450 (1998).

16. K. Kaefer, M. Nardin, K. Blahna, J. Csicsvari, Replay of Behavioral Sequences in the Medial Prefrontal Cortex during Rule Switching. *Neuron* (2020) https:/doi.org/10.1016/j.neuron.2020.01.015.

17. R. J. Douglas, K. A. C. Martin, Neuronal circuits of the neocortex. *Annu Rev Neurosci* **27**, 419–451 (2004).

18. S. Ährlund-Richter, *et al.*, A whole-brain atlas of monosynaptic input targeting four different cell types in the medial prefrontal cortex of the mouse. *Nat Neurosci* **22**, 657–668 (2019).

19. K. L. Agster, R. D. Burwell, HIPPOCAMPAL AND SUBICULAR EFFERENTS AND AFFERENTS OF THE PERIRHINAL, POSTRHINAL, AND ENTORHINAL CORTICES OF THE RAT. *Behav Brain Res* **254**, 50–64 (2013).

20. A. J. Hill, First occurrence of hippocampal spatial firing in a new environment. *Exp Neurol* **62**, 282–297 (1978).

21. M. A. Wilson, B. L. McNaughton, Dynamics of the hippocampal ensemble code for space. *Science* **261**, 1055–1058 (1993).

22. C. Gemmell, M. Anderson, S. M. O'Mara, Deep layer prefrontal cortex unit discharge in a cue-controlled open-field environment in the freely-moving rat. *Behavioural Brain Research* **133**, 1–10 (2002).

23. T. M. Jay, M. P. Witter, Distribution of hippocampal CA1 and subicular efferents in the prefrontal cortex of the rat studied by means of anterograde transport of Phaseolus vulgaris-leucoagglutinin. *J. Comp. Neurol.* **313**, 574–586 (1991).

24. F. Condé, E. Maire-Lepoivre, E. Audinat, F. Crépel, Afferent connections of the medial frontal cortex of the rat. II. Cortical and subcortical afferents. *J. Comp. Neurol.* **352**, 567–593 (1995).

25. L. A. Cenquizca, L. W. Swanson, Spatial organization of direct hippocampal field CA1 axonal projections to the rest of the cerebral cortex. *Brain Res Rev* **56**, 1–26 (2007).

26. X. Liu, A. G. Carter, Ventral Hippocampal Inputs Preferentially Drive Corticocortical Neurons in the Infralimbic Prefrontal Cortex. *J. Neurosci.* **38**, 7351–7363 (2018).

27. A. D. Wagner, *et al.*, Material-specific lateralization of prefrontal activation during episodic encoding and retrieval. *Neuroreport* **9**, 3711–3717 (1998).

28. W. M. Kelley, *et al.*, Hemispheric specialization in human dorsal frontal cortex and medial temporal lobe for verbal and nonverbal memory encoding. *Neuron* **20**, 927–936 (1998).

29. V. Goel, “Chapter 10 - Hemispheric asymmetry in the prefrontal cortex for complex cognition” in *Handbook of Clinical Neurology*, The Frontal Lobes., M. D’Esposito, J. H. Grafman, Eds. (Elsevier, 2019), pp. 179–196.

30. T. Hainmueller, M. Bartos, Parallel emergence of stable and dynamic memory engrams in the hippocampus. *Nature* **558**, 292–296 (2018).

31. C. F. Doeller, C. Barry, N. Burgess, Evidence for grid cells in a human memory network. *Nature* **463**, 657–661 (2010).

32. J. Jacobs, *et al.*, Direct recordings of grid-like neuronal activity in human spatial navigation. *Nature Neuroscience* **16**, 1188–1190 (2013).

33. J. Hawkins, M. Lewis, M. Klukas, S. Purdy, S. Ahmad, A Framework for Intelligence and Cortical Function Based on Grid Cells in the Neocortex. *Front. Neural Circuits* **12** (2019).

34. G. V. Di Prisco, R. P. Vertes, Excitatory actions of the ventral midline thalamus (rhomboid/reuniens) on the medial prefrontal cortex in the rat. *Synapse* **60**, 45–55 (2006).

35. W. B. Hoover, R. P. Vertes, Anatomical analysis of afferent projections to the medial prefrontal cortex in the rat. *Brain Struct Funct* **212**, 149–179 (2007).

36. B. Delatour, M. P. Witter, Projections from the parahippocampal region to the prefrontal cortex in the rat: evidence of multiple pathways. *The European Journal of Neuroscience* **15**, 1400–1407 (2002).

37. K. E. Stephan, *et al.*, Lateralized Cognitive Processes and Lateralized Task Control in the Human Brain. *Science* **301**, 384–386 (2003).

38. R. B. Levy, *et al.*, Circuit asymmetries underlie functional lateralization in the mouse auditory cortex. *Nature Communications* **10**, 2783 (2019).

39. Y. Shinohara, *et al.*, Left-right asymmetry of the hippocampal synapses with differential subunit allocation of glutamate receptors. *PNAS* **105**, 19498–19503 (2008).

40. D. Song, *et al.*, The lateralization of left hippocampal CA3 during the retrieval of spatial working memory. *Nature Communications* **11**, 2901 (2020).

41. O. A. Shipton, *et al.*, Left–right dissociation of hippocampal memory processes in mice. *PNAS* **111**, 15238–15243 (2014).

42. A. Rubin, N. Geva, L. Sheintuch, Y. Ziv, Hippocampal ensemble dynamics timestamp events in long-term memory. *eLife* **4**, e12247 (2015).

43. K. Ohki, S. Chung, Y. H. Ch’ng, P. Kara, R. C. Reid, Functional imaging with cellular resolution reveals precise micro-architecture in visual cortex. *Nature* **433**, 597–603 (2005).

44. M. L. Andermann, C. I. Moore, A somatotopic map of vibrissa motion direction within a barrel column. *Nat Neurosci* **9**, 543–551 (2006).

45. C. Schmidt-Hieber, M. Häusser, Cellular mechanisms of spatial navigation in the medial entorhinal cortex. *Nat. Neurosci.* **16**, 325–331 (2013).

46. J. E. Chung, *et al.*, A Fully Automated Approach to Spike Sorting. *Neuron* **95**, 1381-1394.e6 (2017).

47. A. Sirota, *et al.*, Entrainment of neocortical neurons and gamma oscillations by the hippocampal theta rhythm. *Neuron* **60**, 683–697 (2008).

48. J. A. Gallego, M. G. Perich, R. H. Chowdhury, S. A. Solla, L. E. Miller, Long-term stability of cortical population dynamics underlying consistent behavior. *Nat. Neurosci.* **23**, 260–270 (2020).

49. J. M. Stonehouse, G. J. Forrester, Robustness of the t and U tests under combined assumption violations. *Journal of Applied Statistics* **25**, 63–74 (1998).

Figures and figure legends

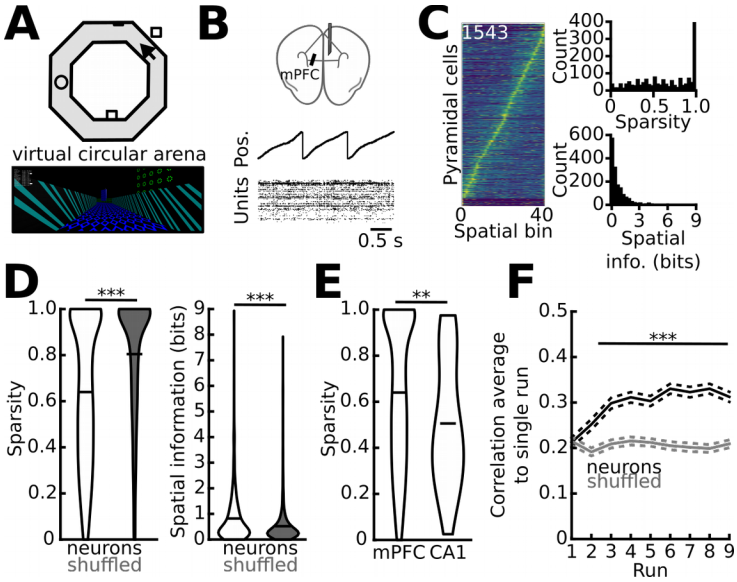

Figure 1: Spatially tuned activity of prefrontal pyramidal neurons during self-paced, unrewarded motion.

(A) Experimental protocol for head-fixed recordings during navigation in the virtual reality. Arrow on the track indicates the position shown at the bottom. (B) Single-unit recording during movement on the track. Black line indicates position on the track. Each row of the raster plot denotes one unit. (C) Left: Spatially binned activity of pyramidal cells (N=17 mice). Right: Histograms of sparsity and spatial information. Low sparsity values indicate stronger spatial tuning. (D) Pyramidal cells show significant spatial tuning compared to shuffled controls. Sparsity: $P=4*10^{-55}$. Spatial information: $P=10^{-21}$. N=1543 units, Welch's tests. (E) Comparison of sparsity between mPFC and CA1 pyramidal cells (N=35 units). P=0.002, Mann-Whitney U-test. (F) Correlation of average spatial tuning to individual runs reveals significant spatial representation from the second lap onwards (run 1: P=0.850, run 2-10: $P=10^{-5}$ to $P=10^{-20}$, Welch's tests). **P<0.01, ***P<0.001. Lines in (D) and (E) show the mean. Data in (F) are mean and sem.

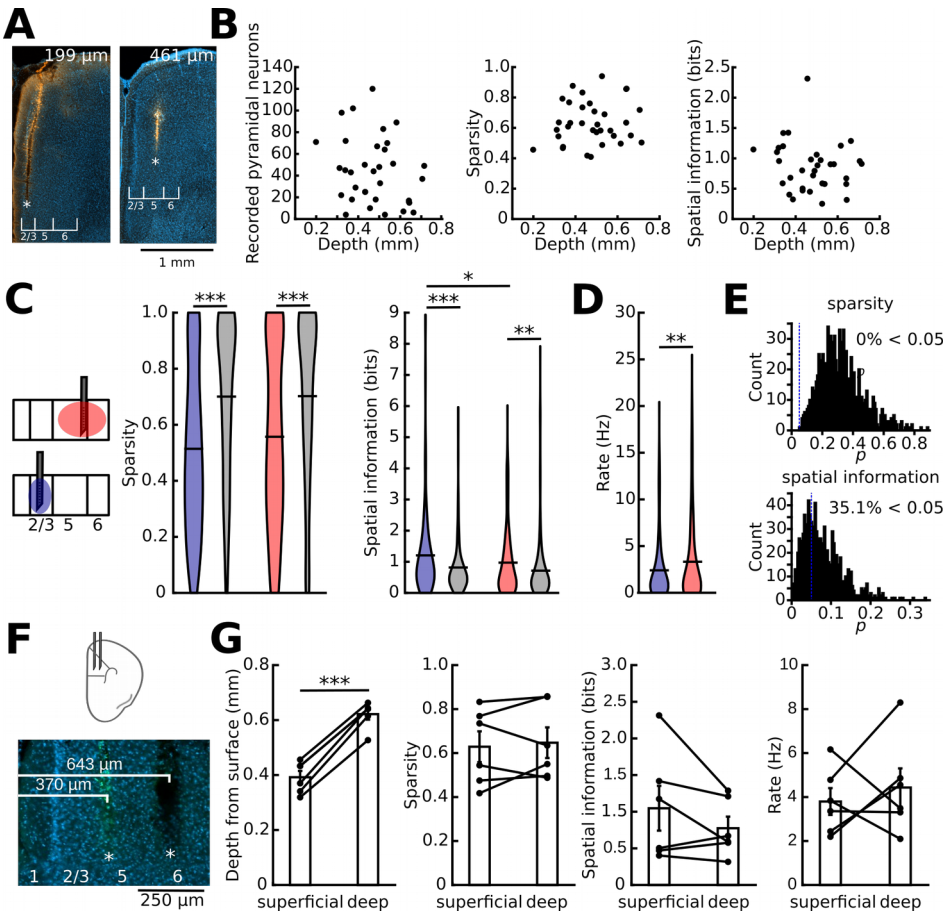

Figure 2: Spatial tuning emerges across cortical layers. (A) Histology of probe tracks located in superficial layer 2/3 (left) and deep layer 5 (right). Values in the top right corner indicate the laminar depth of the recording. (B) The number of recorded pyramidal neurons (left, P=0.198), average sparsity (middle, P=0.621), and average spatial information (right, P=0.257) did not correlate with recording depth. (C) Pyramidal neurons in layer 2/3 and layer 5/6 show significant sparsity and spatial information compared to shuffled controls (layer 2/3: sparsity: $P=1.6*10^{-11}$, spatial information: P=0.0004, N=233 neurons. Layer 5/6: sparsity: $P=1.3*10^{-8}$, spatial information: P=0.002, N=311 neurons, shuffled data in grey). Comparisons between layer 2/3 and 5/6: sparsity: P=0.112, spatial information: P=0.03. (D) Firing rate was significantly higher in deep layers. P=0.007. (E) Rate-matched iterations of sparsity (top) and spatial information (bottom) revealed no significant differences in the majority of cases. (F) Top, schematic of simultaneous recordings with two shanks placed at different cortical depths. Bottom, example of dual-site recording at 370 and 643 µm depth. (G) Left, summary of recording depth of the shanks. Right, there was no differences in sparsity (P=0.629), spatial information (P=0.204) or firing rate (P=0.562) of neurons recorded on superficial and deep shanks. Values are session averages for both shanks. Depth comparison: $P=1.4*10^{-5}$. N=6 sessions from 3 mice. *P<0.05, **P<0.01, ***P<0.001. Lines in (C) and (D) show the mean. Data in (G) are mean and sem.

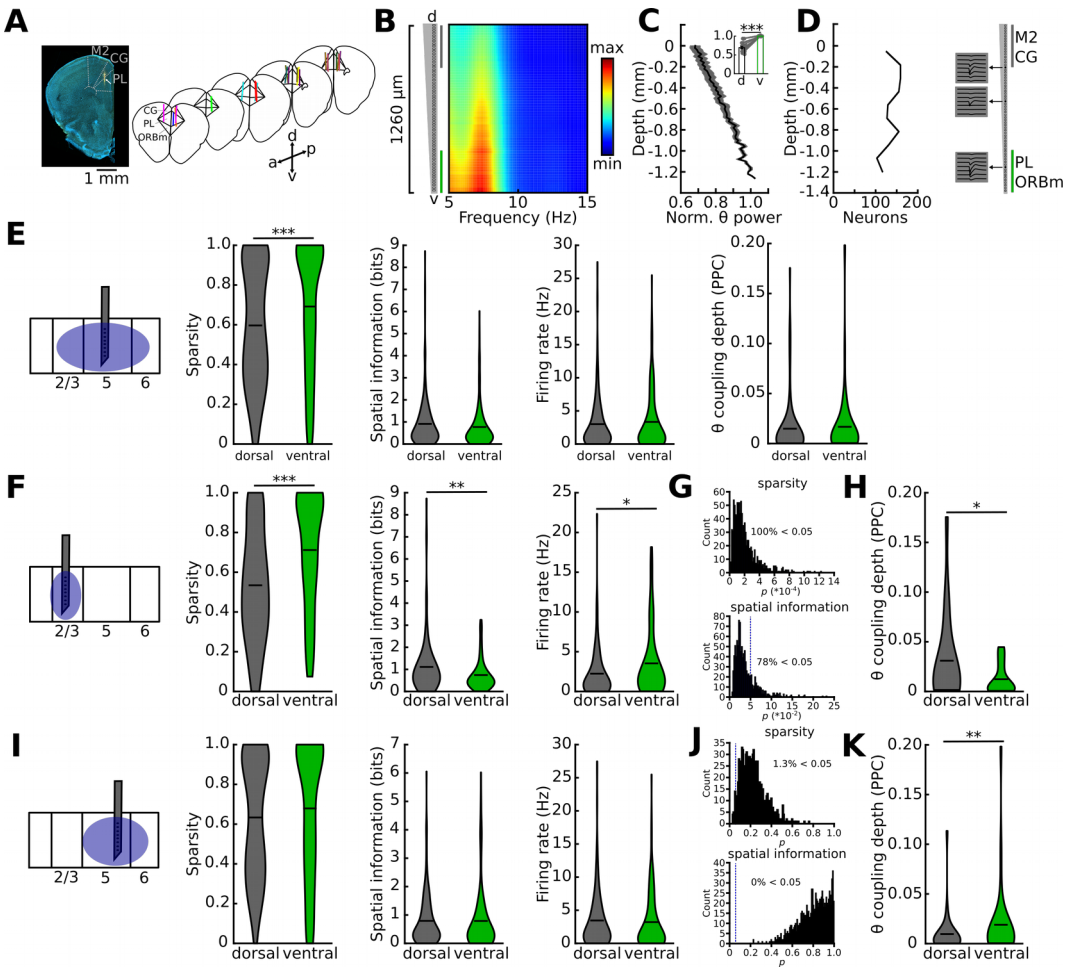

Figure 3: A layer-specific dorso-ventral gradient in spatial representation. (A) Reconstruction of recording sites. Left: DiI-labelled probe track in the prefrontal cortex (arrow). Right: Location of silicon probes. Each mouse is presented in a different color (*N*=14 mice). M2: accessory motor cortex, PL: prelimbic cortex, CG: cingulate cortex, ORBm: medial orbital cortex, a: anterior, p: posterior, d: dorsal, v: ventral. (B) Example of the dorsoventral depth profile of theta power along the shank. (C) Average normalized theta power as a function of d-v depth. Inset: Average normalized theta power of the dorsal five versus the ventral five recording sites. $P=1.2*10^{-9}$, paired *t*-test. (D) Number of recorded neurons along the shank length (10 bins). Right: Identification of unit location along the probe shank. Grey and green depths indicate the locations used for grouping neurons into dorsal and ventral mPFC, respectively. (E) Comparisons of sparsity (*P*=0.0002), spatial information (*P*=0.094), firing rate (*P*=0.326) and theta coupling depth (*P*=0.7) for the top and bottom 300 µm of the shank. PPC: pairwise phase consistency. *N*=337 dorsal and 265 ventral neurons. Welch's tests. (F) The same comparisons for layer 2/3 recordings revealed a prominent d-v gradient in sparsity ($P=6.4*10^{-6}$) and spatial information (*P*=0.007) and a difference in firing rate (*P*=0.011). N=125 dorsal and 104 ventral neurons. Welch's tests. (G) Rate-matched iteration test revealed significant d-v gradients for sparsity and spatial information in the majority of iterations. (H) A d-v gradient in theta coupling strength. *P*=0.035, *N*=18 dorsal and 31

ventral neurons. Mann-Whitney U-test. (I-K) Same as (F-G), but for deep layer recordings. There was no significant d-v gradient in sparsity (P=0.176), spatial information (P=0.972) or rate (P=0.592). N=212 dorsal and 161 ventral neurons. Welch's tests. Theta coupling depth was significantly higher in ventral vs. dorsal neurons (P=0.003). Mann-Whitney U-test. N=56 dorsal and 60 ventral neurons. *P<0.05, **P<0.01, ***P<0.001. Lines in (E), (F), (H), (I), and (K) show the mean. Data in (C) are mean and sem.

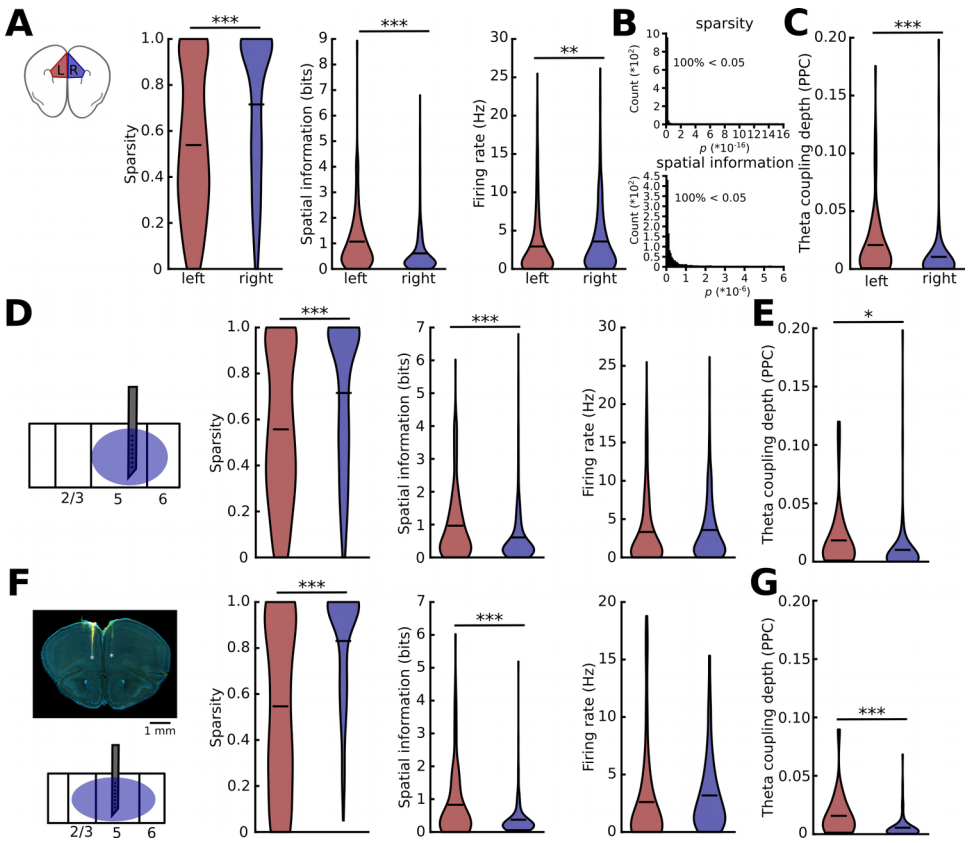

Figure 4: Stronger spatial tuning in the left hemisphere. (A) Pyramidal neurons recorded in the left mPFC showed lower sparsity (P=8*10^{-22}), higher spatial information (P=4*10^{-13}), and lower firing rates (P=0.008). N=544 pyramidal cells from the left and N=639 from the right, 11 and 8 mice, Welch's tests. (B) Rate-matched iterations to account for firing rate differences revealed significantly different sparsity and spatial information in all cases (1000 iterations). (C) Pyramidal cells of the left hemisphere showed stronger coupling to theta oscillations (P=0.004, Welch's test). N=100 left and 203 right neurons. (D) Left-dominant spatial representation was evident in deep layer recordings. Sparsity: P=2*10^{-12}, Spatial information: P=4*10^{-7}, Firing rate: P=0.407, Welch's tests. N=311 pyramidal cells from the left and N=639 from the right, 7 and 8 mice. (E) Same as (C) but for layer 5/6 recordings. P=0.046, Welch's test. N=61 left and 203 right. (F) Left: Probe tracks of recordings from the left and right mPFC during subsequent sessions from the same animal. Right: Left-dominant spatial representation was evident when restricting the analysis to animals in which sequential left-right or right-left recordings were performed. Sparsity: P=1*10^{-14}, Spatial information: P=5*10^{-6}, Firing rate: P=0.167, Welch's tests. N=142 pyramidal cells from the left and N=213 from the right, 3 animals. (G) Same as (E) but for sequential recordings. P=3*10^{-5}. N=23 left and 96 right neurons. Mann-Whitney U-test. *P<0.05, **P<0.01, ***P<0.001. Lines in violin plots show the mean.

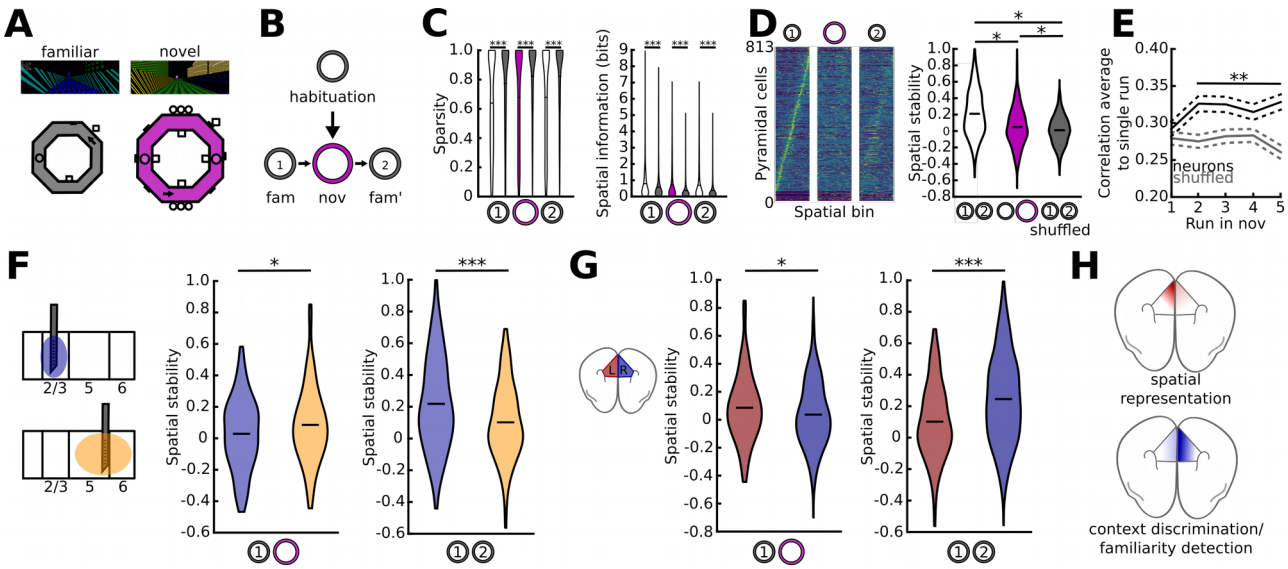

Figure 5: Multiple topographical gradients of spatial pattern reactivation during re-exposure to a familiar environment.

(A) Animals were sequentially exposed to a familiar (left, grey) and novel track (right, purple). Bottom: Schematic of the two tracks. Arrows indicate position of the views shown on top. (B) Schematic of the recording paradigm. (C) Sparsity (values for fam, nov and fam': $P=10^{-22}$, 10^{-20}, 10^{-20}) and spatial information ($P=10^{-5}$, 10^{-13}, 10^{-10}) compared to shuffled controls (grey, N=813 units from 8 mice, Welch's tests). (D) Left: Spatial maps of all pyramidal cells during fam, nov and fam' sorted by position of peak activity during fam. Plots are shown with the same sorting. Right: Spatial stability (i.e. spatial correlation) between fam and fam', fam and nov, and for shuffled spike trains (N=813 units form 8 mice, Tukey's tests). (E) Correlation of average spatial tuning to individual runs during nov revealed significant spatial representation from the second lap onwards (run 1: P=0.336, run 2-5: P=0.002 to $P=1.2*10^{-6}$, Welch's tests). (F) Spatial stability is higher between fam and nov (P=0.047) but lower between fam and fam' (P=0.0003) in layer 5/6 compared to layer 2/3. N=162 superficial and 142 deep neurons, Welch's tests. (G) Higher spatial stability to nov in the left (P=0.045) but stronger reactivation of spatial tuning during reexposure to fam' in the right hemisphere ($P=2.9*10^{-8}$). N=142 left and 509 right neurons, Welchs tests. (H) Schematic of the proposed role of prefrontal subfields: Dorsal areas of the left mPFC contribute more strongly to spatial representation, while superficial layers of the right mPFC support context discrimination and familiarity detection. *P<0.05, **P<0.01, ***P<0.001. Lines in violin plots show the mean. Data in (E) are mean and sem.

Author contributions

J.-F. S. and M.B. designed the study, J.-F. S. performed experiments and analyzed the data, J.-F. S. and M.B. wrote the manuscript.

Declaration of interests

The Authors declare no competing interests.